Materials Science & Engineering A 706 (2017) 227–235

Contents lists available at ScienceDirect

Materials Science & Engineering A

journal homepage: www.elsevier.com/locate/msea

Effect of machined feature size relative to the microstructural size on the superelastic performance in polycrystalline NiTi shape memory alloys

Partha P. Paul[a,*], Harshad M. Paranjape[b], Behnam Amin-Ahmadi[b], Aaron P. Stebner[b], David C. Dunand[c], L. Catherine Brinson[a,c]

[a] Mechanical Engineering, Northwestern University, Evanston, IL 60201, United States
[b] Mechanical Engineering, Colorado School of Mines, Golden, CO 80401, United States
[c] Materials Science and Engineering, Northwestern University, Evanston, IL 60201, United States

ARTICLE INFO

Keywords:
Nickel titanium
Shape Memory Alloys
Digital image correlation
Electron back scattering diffraction
Size effects

ABSTRACT

This study demonstrates a transition from a structure-dominated response to a microstructure-dominated response around machined features in a polycrystalline NiTi shape memory alloy (SMA), as the size of the features relative to the mean grain size is varied. The specific structural features considered are a pair of holes of varying separation and size in the 100–500 micrometer range. The local deformation around the holes is experimentally characterized during superelastic loading and compared with the predictions of a macro-scale phenomenological model for phase transformation. This comparison, coupled with a microstructural analysis reveals two key results. In the case when the holes are much larger than the grains, the local strain fields are predominantly determined by the stress concentrations around the structural features, and they are adequately predicted by the phenomenological model. However, when the holes and the grains are of comparable size, microstructural heterogeneity and fine-scale microstructural features such as precipitates determine the local superelastic response. The prediction of the macro-scale model in this case significantly deviates from the experimental observation. A key outcome of this work is a criterion in terms of the microstructure and the relative structural feature size in SMAs for determining the applicability of macro-scale models vs. micromechanical models of phase transformation for predicting the local deformation response.

1. Introduction

Shape Memory Alloys (SMAs), which derive their remarkable properties from a martensitic phase transformation, have received broad attention to understand the mechanics and crystallography of phase transformation [1,2] and the effect of processing parameters on the performance [3–5]. These efforts can be divided into two broad categories, based on the relative length-scale of the extrinsic structural features (such as pores, cavities and cracks) and the microstructural features (such as grain morphology and orientations) in the specimens studied. Mechanics of SMAs at length scales where the size of the specimen or any machined features is sufficiently larger than the grain size allows for the assumption of spatially homogeneous and occasionally isotropic material properties. This length-scale has historically received extensive attention in terms of both modeling and characterization. However, at a length-scale of the structural features approaching the intrinsic microstructural length, material properties are heterogeneous (e.g., the crystal orientation abruptly changes from one grain to another) and consequently interpretation of the local phase transformation response must take into account these heterogeneities.

Experimentally, phenomena such as the dependence of transformation stress and recoverable strain on texture and crystal orientations [6–8], anisotropy in the elastic modulii of austenite and martensite [9–11], relative stresses for the onset of phase transformation, reorientation, plasticity and their relative strain contribution [12] have been studied extensively using various diffraction techniques and in-situ testing. Common to these studies is the assumption that the volume interrogated contains a large number of grains and the observed response is not dependent on individual grain responses or on microstructural heterogeneities, but rather on volume-averaged, representative material parameters. Similarly, the observed response is insensitive to the specimen size. However, size effects become observable as the specimen size is decreased. Particularly as the specimen size approaches the microstructural length scales, the size effects become prominent. When the microstructural length scale is measured in terms of the average grain size, this spans from the nanometer to

* Corresponding author.
E-mail address: parthapaul2018@u.northwestern.edu (P.P. Paul).

http://dx.doi.org/10.1016/j.msea.2017.09.016
Received 8 May 2017; Received in revised form 28 August 2017; Accepted 5 September 2017
Available online 07 September 2017
0921-5093/

micrometer range in most metals and alloys.

Experimental studies conducted on SMA wires with various diameters, micrometer and nano-sized pillars, and polycrystals with nanometer to micrometer-sized grains have revealed a change in the transformation mechanics as the intrinsic size is reduced. For example, experiments on Cu-based SMA show that thermal effects related to heat transfer from the wire to the surroundings play a role in determining critical transformation stress and hysteresis when the wire diameter is large (hundreds of microns). However, in thinner wires (1–100 μm), the heat transfer is near-instantaneous and the transformation kinetics is dominated by granular constraints and pinning at free surfaces. The result is a higher hysteresis width in thinner wires due to a larger relative free surface area to provide pinning sites. Another manifestation of this size effect is a transition from many martensite domains to a single domain microstructure with decreasing intrinsic size [13]. At even smaller length scales, in micro and nano-pillars, the onset of transformation is sudden [14] and its progression seen to occur in a non-smooth manner and the hysteresis shows a non-intuitive relation with the thermal cycling rate – it decreases with higher thermal cycling rates [15,16]. Structure-property relationships are seen to be very different in nanocrystalline NiTi wires, as compared to conventional wires, with an increased fatigue damage resistance and recoverable strain in wires with nano-sized grains [17]. An extreme manifestation of the size effects occurs at the length scales smaller than 200 nm in NiTi SMAs, where the phase transformation is completely suppressed in very small grains [18,19].

A distinction between length scales is essential to reliably predict the thermo-mechanical response of SMAs depending on the specimen size. This distinction is reflected in the numerical models for SMAs. At the macro-scale, phenomenological or self-consistent models are suitable to predict the thermo-mechanical response on cycling, multi-axial loading behavior, and contributions from multiple inelastic mechanisms – phase transformation, reorientation, detwinning and plasticity [20–27]. These models, while being computationally efficient, do not account for microstructural heterogeneity. Micromechanics based approaches, in contrast, are able to capture the effect of microstructure and simulate the local SMA response [28–33]. These approaches are suitable to predict the performance and microstructural evolution at the micro to nano length scales. While it is appealing to use these micromechanical approaches to model SMA behavior of aggregates with millions of grains, it is not practical due to prohibitive computational expense. Hence it is necessary to make a choice between the two approaches depending on the required level of detail in the predicted response.

To make such a choice between phenomenological and micromechanical models, an understanding of the role played by the size of structural features (e.g., machined holes, pores, notches) and individual grains in polycrystal deformation is necessary. Previous endeavors on studying the effect of structural features include: (i) a numerical exercise to understand the coupling of elastic and inelastic strain fields locally around a single machined hole and hole assemblies using a phenomenological model [34], and (ii) a comparison to experimental strain fields around a single hole using digital image correlation, when the hole is much bigger than the mean grain size [35]. While empirical studies on wires with micron-scale diameter and *bamboo* grain morphology address some of the issues related to the size effects when the grain and structural sizes are similar, there are several open questions. The influence of grain interaction on SMA deformation has been explored numerically [36] and empirically [37,38], however the nature of granular interaction is not clear when the specimen or the features in it are of comparable size to the grains themselves. The role played by microstructure vs. the stress concentration in a small specimen or around small structural features in determining the local superelastic response is unclear. With the increasing interest in miniature SMA components, including micro electro-mechanical systems and porous SMA assemblies where the pore size can be comparable to the grain size, a quantitative understanding of the deformation phenomena at the intermediate length scales is essential.

This work explores the SMA mechanics at the intermediate length scale where the structural feature size approaches the microstructural length scale. Using three specific cases, we vary the size of machined features (micro-holes) in SMA specimens until the micro-hole diameter is comparable to the average grain size. We track the local and global strain fields during superelastic loading using digital image correlation (DIC), a technique that has been extensively used to characterize the SMA deformation at the micro and macro length scales [35,39,40]. By comparing the measured surface deformation with the prediction of a macro-scale, phenomenological model, we are able to identify a length scale at which the phenomenological prediction significantly deviates from the measured strain. This is the length scale at which the microstructure starts to play a significant role in determining the local deformation, rather than the homogeneous material properties or the boundary conditions. Hence the key outcome of this work is a criterion in terms of relative length scales of specimen, structural features, and microstructure, to determine the propriety of phenomenological vs. microstructural modeling approaches for predicting SMA deformation.

2. Materials, experiments and simulations

2.1. Material and sample description

A polycrystalline NiTi plate (Ti-50.53at%Ni) supplied by Confluent Medical Technologies (formerly Nitinol Devices and Components) was used to prepare three planar dogbone specimens with 25 mm × 3 mm gage dimensions according to the ASTM E8 standard [41]. The transformation temperatures were determined by differential scanning calorimetry (DSC), using a Mettler Toledo DSC822^e calorimeter to be A_s = 293 K, A_f = 303 K from the heating curve and M_f= 255 K, M_s = 278 K, R_s = 283 K and R_f = 293 K from the cooling curve. The dogbone specimens were cut using electrical discharge machining and subjected to a high temperature anneal at 1200 K for 900 s in vacuum and oven cooling to room temperature. Then a second anneal at 773 K in air for 1800 s with the specimens sandwiched between heavy steel plates to ensure that the specimens did not warp during annealing, followed by a low temperature anneal at 473 K for 86.4 ks. The surface was then ground and polished up to 1 μm using a diamond-based solution, followed by vibratory polishing with 0.06 μm colloidal silica.

Tensile testing was performed on each of the following three dogbone specimens.

MONOLITH This sample has a monolithic gage section without any machined holes.

S550 This sample has two 564 μm diameter holes machined in the center of the gage with 970 μm center-to-center spacing.

S150 This sample has two 156 μm diameter holes with a 266 μm center-to-center spacing in the center of the gage.

The dimensions of these specimens are summarized in Table 1, and the specimen geometries are schematically shown in Fig. 1(a).

To ensure repeatability of the results, additional samples with similar hole diameters to S550 specimen were tested and demonstrated similar results in terms of the macro stress-strain response to the key

Table 1
Dimensions of the planar dogbone specimens used to perform tension tests. D, t, d, and L are schematically shown in Fig. 1(b).

Name	Width (D, mm)	Thickness (t, mm)	Hole Diameter (d,μ m)	Hole Spacing (L, μ m)
MONOLITH	3.02	0.70	–	–
S550	2.99	0.44	564	970
S150	3.02	0.59	156	266

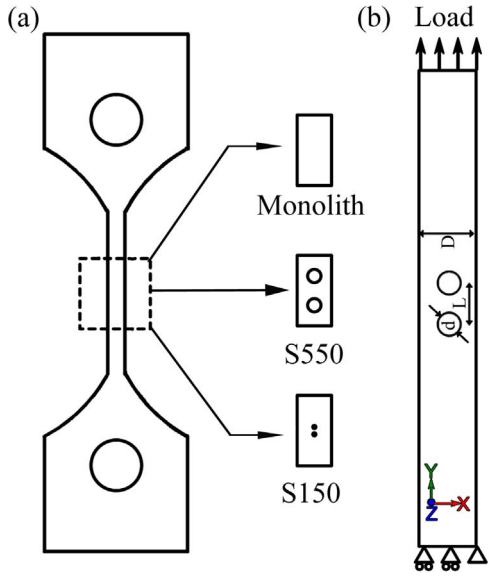

Fig. 1. (a) Schematic of the tensile dogbone specimens with the details of the machined hole geometry. (b) Boundary conditions employed in the finite element analysis (FEA). The same boundary conditions are employed in all the simulations.

findings in Section 3 and Section 4. However, the results for those additional specimens are not shown.

2.2. Tension experiment setup

The specimens were loaded in tension at room temperature to 0.75% global axial strain under displacement control at an engineering strain rate of $2 \times 10^{-4}\ s^{-1}$ and then unloaded to zero load. The loading was done using a Sintech 20 G load frame and the global strain was measured using a 1 mm knife-edge extensometer.

Local strains around the holes were measured using a digital image correlation (DIC) setup consisting of a Point Grey Grasshopper (9.1 MP) camera with a K2 Distamax Long Distance Microscopic lens. DIC is a non-contact method for the measurement of surface strains by tracking the movement of patterns on the specimen surface and has been used extensively to measure strain distributions in SMA specimens [42,43]. A grey layer of paint primer was used as the background layer and 5 μm alumina particles were then sprayed on the wet primer to obtain a speckle pattern. A sequence of images of the gage section captured at 1 frame per second during loading and unloading for each specimen was then analyzed through VIC2D software from Correlated Solutions to obtain the local axial strains.

2.3. Microstructural analysis

Grain orientation distribution and mean grain size in the representative regions in each specimen were obtained by electron backscatter diffraction microscopy (EBSD) using a FEI Quanta 600F electron microscope. These measurements were performed prior to tension testing. Post-mortem transmission electron microscopy (TEM) analysis of the S150 sample was performed using FEI Talos (FEG, 200 kV) to characterize the phases and precipitates present. The location for TEM analysis was chosen based on the EBSD data such that a $<111>_{B2}$ zone axis was aligned in the TEM. A cross-sectional TEM thin foil was prepared using the Focused Ion Beam (FIB) lit-off technique and bright field and selected area diffraction pattern (SADP) of the sample were obtained.

2.4. Simulations using a phenomenological model for phase transformation

The superelastic response during the tension experiments for each specimen was simulated using a macro-scale, phenomenological model consisting of elastic and phase transformation constitutive laws. This model uses a constant Lagrange multiplier based explicit integration scheme for reduced computational expenses. The model and its Abaqus user material (VUMAT) implementation are described in detail elsewhere [44], however the key features of the formulation are:

1. The representative volume element (material point) is assumed to be a polycrystal with isotropic elastic properties and a uniform maximum transformation strain (ε_{tr}^{max}).
2. The total strain ε at a material point is additively decomposed into an elastic (ε_e) and a transformation component (ε_{tr}) as: $\varepsilon = \varepsilon_e + \varepsilon_{tr}$.
3. The volume change on transformation from austenite to martensite phase is assumed to be negligible as is the standard assumption of the Crystallographic Theory of Martensite [2].
4. Martensitic transformation is tracked through two internal variables: self-accommodated martensite volume fraction (ξ_{SA}) and oriented martensite volume fraction (ξ_σ). The total martensite volume (ξ) fraction is the sum of these two components: $\xi = \xi_{SA} + \xi_\sigma$.
5. Only the oriented volume fraction of martensite contributes to the transformation strain.
6. A phenomenological expression for the driving force for phase transformation is constructed as a function of the deviatoric stress, temperature, and the oriented martensite volume fraction.

The finite element mesh in each case was constructed using 4-node bilinear *plane stress* quadrilateral reduced integration elements (CPS4R in Abaqus notation). The MONOLITH specimen had the same element size throughout the sample (100 elements along the 25 mm gage length). In the case of specimens with holes, a finer finite element mesh was constructed near the holes with a gradual transition to a coarser mesh near the sample edges. For the S150 and S550 samples, at the gage center, the mesh was seeded such that the density of the nodes along the holes remained the same (52 elements along the circumference of the holes). A convergence study was conducted on all the samples to ensure that the mesh was sufficiently resolved, especially near the holes. Since this model does not take any micromechanical inputs, the size of the elements with respect to the average grain size of every specimen is not considered. The boundary conditions imposed in the simulations are shown in Fig. 1(b). They include a rolling boundary conditions on one edge perpendicular to the loading direction to constrain that edge in the direction of loading, a pinned corner of the sample to prevent rigid body modes and a uniform displacement applied to all nodes on the other edge, to mimic the experimental loading.

The elastic stiffness, onset stress for forward and reverse transformation, and the hardening parameters for the forward and reverse transformation were calibrated using the global stress-strain curve obtained for the MONOLITH specimen. Strain along the loading direction and martensite volume fraction were recorded from each of the simulations. The simulated global stress-strain curves are obtained from the displacements at points corresponding to the location of the edges of the extensometer and the reaction forces obtained from the loading edge of the finite element analysis (FEA) model geometry considered. Table 2 summarizes the calibrated model properties and material parameters used in the simulations. The parameters include kinetic parameters (A_r), internal parameters (C^r, C^f) and hardening co-efficients (H_σ, K).

3. Results

3.1. MONOLITH sample

Fig. 2 shows the experimental (solid curve) and simulated (dotted curve) global stress-strain response for the MONOLITH sample during a uniaxial tension test. In the experimental curve, during loading, a nonlinearity appears at a global strain between 0.45% and 0.5%. The

Table 2
Calibrated material properties and model parameters for the simulations.

Property	Symbol	Value	Parameter	Value
Young's modulus	E	32 GPa	Y_{re}	40 MPa
Poisson's ratio	ν	0.4	H_σ	4000 J kg^{-1}
Density	ρ	6.45 gm cm^{-3}	C^f	105 MPa
Martensite start	M_s	278 K	C^r	2 MPa
Martensite finish	M_f	255 K	A^r	2 MPa
Austenite start	A_s	293 K	K	1 MPa
Austenite finish	A_f	300 K		
Patel-Cohen coeff.	$C_{A,M}$	4.5 MPa K^{-1}		
Max. trans. strain	ε_{max}	0.04		
Yield stress	σ_0	1000 MPa		
Initial martensite fraction	ξ_0	0		

transition in the slope of the experimental curve is gradual vs. an abrupt transition in the simulated response. Martensite phase fraction values from the simulation show that this transition represents the onset of phase transformation. The stress-strain curves are hysteritic, and on unloading, the strain completely recovers. At four representative points marked 1–4 on the curve in Fig. 2, the experimentally observed local axial strain distribution in the dogbone gage center is shown in the top row. The local strain gradually increases to a maximum of approximately 0.85% at the peak imposed global strain. At peak global strain, the variation in the local strain is ≈0.4%. For the unloading part, DIC strain measurement shows a gradual reduction in strain to approximately 0% (not shown in the figure). The middle row shows the axial strain distribution from the FEA simulation. The phenomenological model naturally shows a more homogeneous strain distribution as compared to the experiment. The average simulated axial strain at the peak is 0.75%.

3.2. S550 sample

Fig. 3 shows the global axial stress-strain response for the S550 sample, as obtained from the experiment (solid curve) and from the simulation (dotted curve). The experimental stress-strain curve transitions to a non-linear response between 0.35% and 0.4% axial strain, which is smaller than 0.5% for the similar transition for the MONOLITH specimen. The peak global stress for this case is 250 MPa, which is higher than the peak stress of approximately 220 MPa for the MONOLITH specimen. The global strain shows near complete recovery on unloading with less than 0.01% residual strain at 0 load. The local axial strain distribution measured using DIC at four representative points 1–4) is shown in the top row. At point 2, shortly after the onset of non-linearity in the global stress-strain curve, two bands of larger local axial strain emanate from the holes and travel to top-right and bottom-left corners of the gage. With increasing global strain, the local axial strain in these two bands grows until it reaches ≈ 3% at peak global strain. The axial strain away from the holes, in the left and the right regions of the DIC area is near 0%.

The peak stress is underestimated by the phenomenological model (200 MPa), as compared to the experimentally obtained stress value (250 MPa). Plausible reasons for this difference include local plasticity around the holes leading to toughening of the sample and a lack of microstructural input to the FE model. However, it is to be noted that this difference in the macro stress-strain response is not expected to have any influence on the local stress-strain measurement or behavior around the holes, which is the focus of the following sections.

Local FEA axial strain results for the S550 specimen are shown in the middle row over the global curves. The model predicts the formation of "V" shaped bands emanating from each hole. The strain bands have two axes of symmetry: a horizontal axis passing through the center of both holes and a vertical axis passing through the mid-point between two holes. The axial strain in the bands varies between approximately 1% and 2%. There is a strain maximum predicted just above and below each hole and a broad region of strain minimum is predicted between the two holes. Though the local FEA results for the unloading part are not shown, they show a gradual reduction in the axial strain with full strain recovery on unload.

3.3. S150 sample

Fig. 4 shows the macro stress-strain response for the S150 specimen, as measured experimentally (solid curve), and obtained through the simulation (dotted curve). The global experimental response is similar

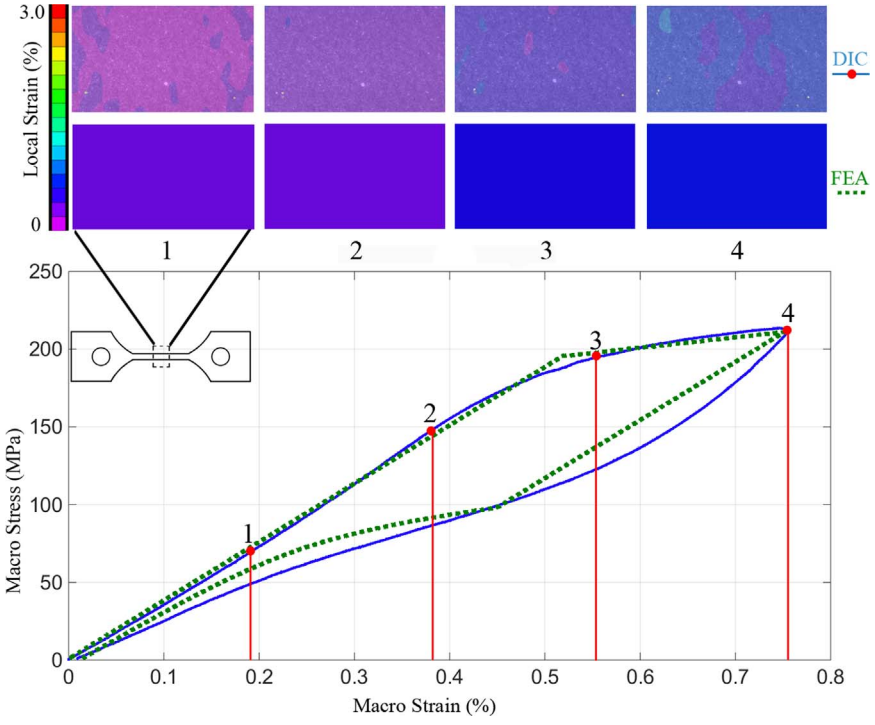

Fig. 2. MONOLITH specimen. Global stress-strain curves and local strain maps obtained from the experiments (solid curve and top row), and macro-scale simulations (dotted curve and bottom row). At peak load, the specimen shows a maximum DIC strain of ≈ 0.85%.

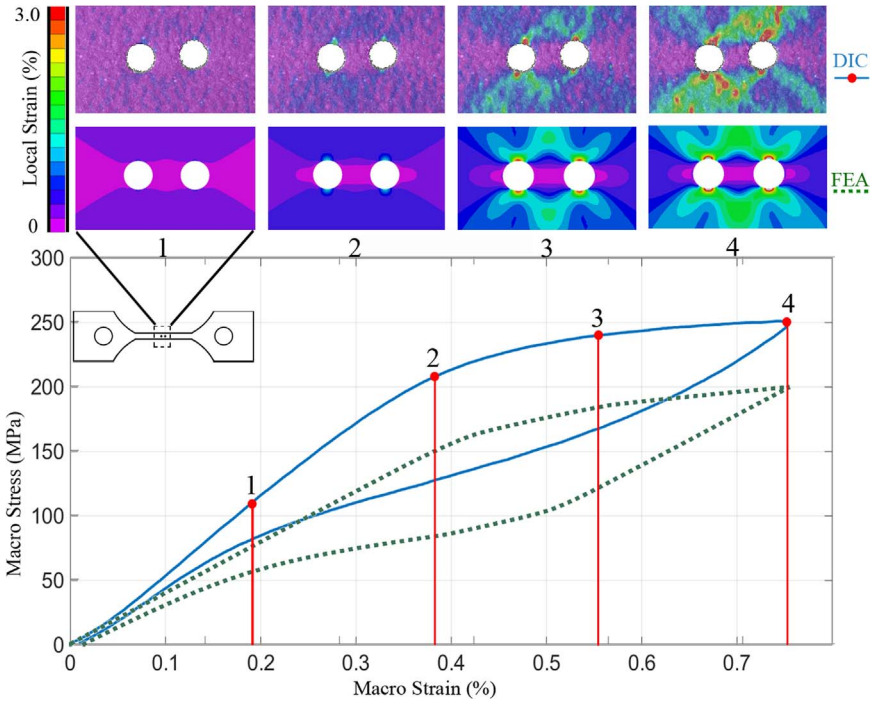

Fig. 3. S550 specimen. Global stress-strain curves and local strain maps obtained from the experimental results (solid curve and top row) and simulated response (dotted curve and bottom row). At peak load, the specimen shows a maximum DIC strain of ≈ 3%. Both experiment and simulation show the formation of strain bands around the holes.

to the MONOLITH specimen. However, a small residual strain (≈ 0.02%) at the end of unloading is observed. The axial strain distribution in the center of the gage, measured using DIC, is shown in the top row. The axial strain is uniform. The average axial strain around the holes at the peak global strain is in fact comparable to the imposed global strain. No strain localization around the holes is observed.

Simulated macro stress-strain response for S150 is shown by the dotted curve, and the local strain map around the holes in the gage is shown in the middle row of Fig. 4. Similar to S550 simulation, a pronounced strain minimum between the holes and the formation of symmetric "V" shaped bands of relatively larger strain around the holes, is predicted for S150. The bands grow perpendicular to the loading direction with increasing global strain.

3.4. Microstructural characterization

Fig. 5 (a-c) show the gage-section microstructures for the MONOLITH, S550, S150 specimens respectively. The grain orientation distributions in terms of inverse pole figure maps are shown in the inset for each subfigure. The grain orientations show a random texture. The mean grain size, calculated using the linear intercept method, in the MONOLITH, S550 and S150 specimens is approximately 50 μm, 87 μm, and 50 μm respectively. The grain structure around the holes is similar compared to that away from the holes. In the S550 specimen, there is some grain refinement between the holes to a mean grain size of approximately 50 μm. However, we do not expect this to affect the response of the material, as this size is well below the grain size where the

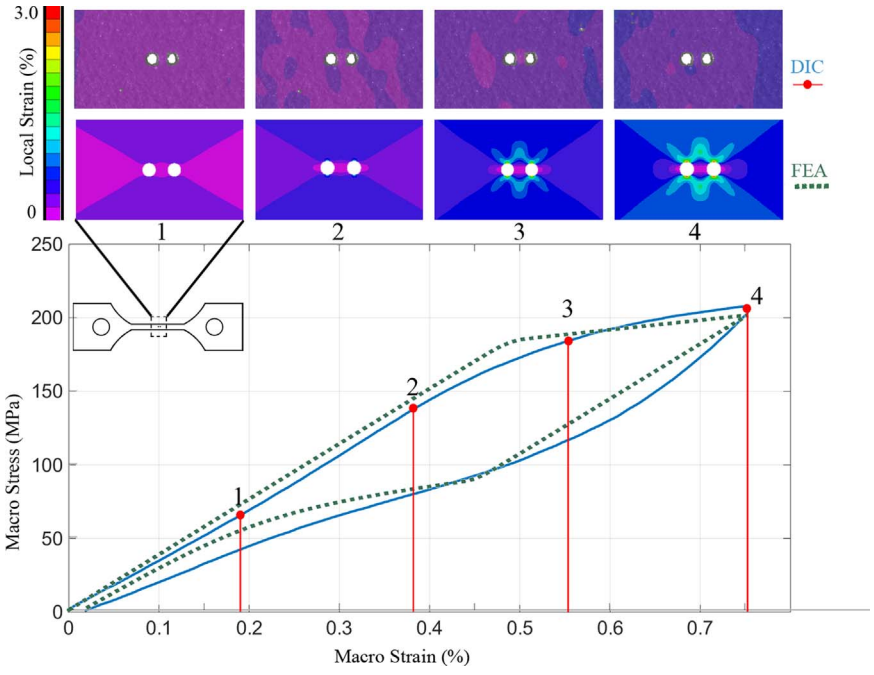

Fig. 4. S150 specimen. Stress-strain curves and local strain maps obtained from the experiment (solid curve and top row) and simulation (dotted curve and middle row). At peak load, the specimen shows a maximum DIC strain of ≈ 0.8%. The experimental response does not show any strain localization around the holes, while the simulated response shows the formation of "V" shaped strain bands.

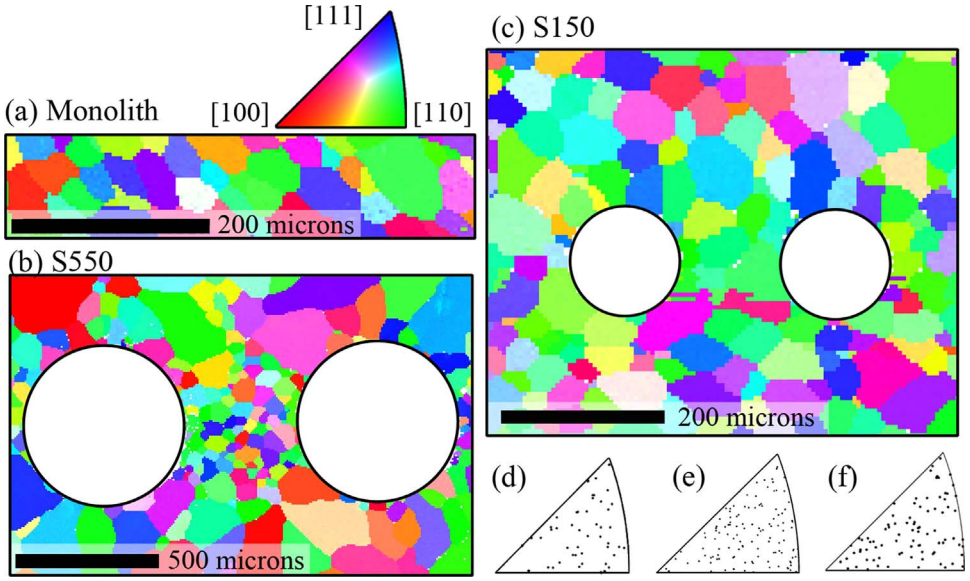

Fig. 5. Grain maps and orientation data (a-c) and mean grain orientation distributions with respect to the loading axis (d-f) for MONOLITH, S550 and S150 specimens respectively, obtained using EBSD. The grain size distribution is similar across the specimens and the texture is random.

Hall-Petch effect begins to be observed. In SMAs, size of grains is expected to play a role in the deformation behavior in the *nanometer regime*, by affecting the transformation onset stress and transformation strain produced [45] or causing the suppression of phase transformation altogether [13]. The grain sizes considered in this work are well above the nanometer scale and we do not expect to see noticeable effects from the grain size.

4. Discussion

A comparison between the spatial distribution of the experimentally measured axial strain and the simulated axial strain in all specimens indicates a trend. The agreement between the model and the experiments decreases as the size of the machined features is reduced from MONOLITH to S150. This suggests that the influence of the microstructural features relative to the effect of the structural features increases as the size of the holes is reduced to approach the average grain size in the specimens. In this section, we discuss the role of the most important structural factor – the presence of holes, relative to the role of microstructural factors, in determining the local strain distribution in each specimen. The microstructural factors considered include the grain structure and any presence of precipitates and secondary phases.

4.1. Effect of relative microstructural size and hole size on strain distribution

4.1.1. Structural factors determine the strain distribution in MONOLITH

For the MONOLITH specimen, the local axial strain distribution at the peak macro strain in the experiments (Fig. 2) shows a relatively small variation (mean 0.8%, standard deviation 0.2%) compared to other specimens. The area in Fig. 2 where the axial strain distribution is reported, is approximately 3 × 2 mm. The mean grain size (diameter) in that specimen is approximately 50 μm. Thus the imaged area consists of approximately 3000 grains. Presence of such large number of grains in the imaged region is expected to smear out the heterogeneous transformation strains in the individual grains.

The experimental MONOLITH stress-strain response shows a gradual change in slope at approx. 0.5% strain. Such transition is typically associated with the onset of phase transformation. This is consistent with the experimental results obtained by Brinson et al. [46] and the simulations of Manchiraju and Anderson [31], where the global stress strain curve shows a gradual transition into the transformation regime. Since grains with varying orientations are present in the specimen, phase transformation initiates in favorably oriented grains. With the increasing imposed strain, phase transformation progressively begins to occur in less favorably oriented grains. Thus the experimental slope gradually decreases as more and more grains start transforming. This phenomenon is not captured in the macro-scale simulation results as the model is agnostic of the microstructure-level progression of phase transformation. Thus in the MONOLITH specimen:

Presence of holes : Not applicable. But the imposed boundary conditions (i.e., the imposed macro strain) determined the observed response.

Microstructure did not have specific effect on the local strain response. However, the interaction between grains introduced a gradual change in slope in the macro stress-strain response.

4.1.2. Structural factors determine the strain distribution in s550 and an influence of the microstructure is apparent

Addition of the structural features in the S550 specimen introduces heterogeneity in the observed strain response. The main source of heterogeneity is the stress concentration around holes. This results in the axial strain concentration of approximately 3% around the holes. This structural effect is captured by the phenomenological model as shown in the simulated local strain plots in Fig. 3 (middle row). While the formation of strain bands is anticipated due to the stress concentration around holes, the experimentally observed bands are asymmetric. A similar observation of asymmetric strain bands around machined holes was made by Bewerse et al. using optical microscopy [35]. This departure from symmetry can be attributed to the influence of the microstructure.

A strain band emanating from the left hole in the S550 specimen is interrupted by a group of grains unfavorably oriented for transformation. Fig. 6(a) shows the DIC strain map for S550 at the peak load. The V-shaped strain band starting from the left hole is interrupted in the top-left corner of the figure. This region is marked by slant lines. The EBSD grain map for the specimen is shown in Fig. 6(b). Several grains with a [1 0 0] orientation are situated in the same region where the strain band is interrupted. According to the Crystallographic Theory of Martensite (CTM) [2], [1 0 0] orientation in NiTi produces a smaller axial transformation strain compared to e.g., [1 1 0] or [1 1 1] orientations. Thus the interrupted strain band is likely the result of the [1 0 0] oriented grains present in that region. Since the phenomenological model does not incorporate any microstructural inputs, the strain concentration in Fig. 3 is symmetric. Based on this information, grain

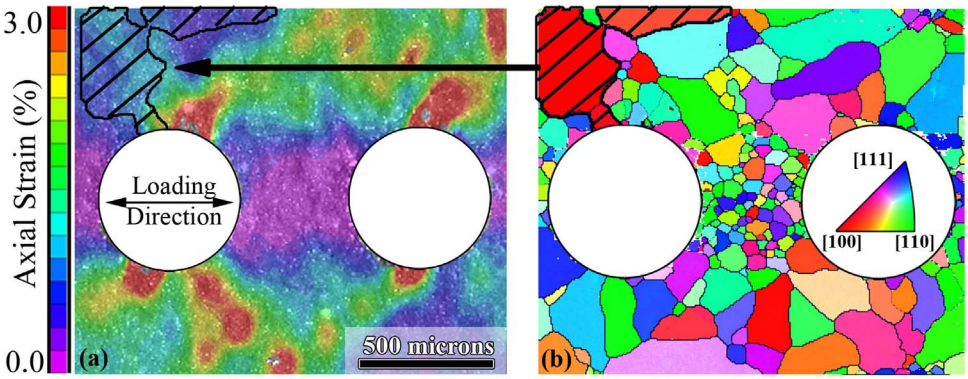

Fig. 6. S550 specimen. (a) Experimental axial strain at peak load with the overlaid boundary of a group of [0 0 1] oriented grains. (b) EBSD grain map showing the [0 0 1] grains in the top-left corner. The grains are marked with slant lines. According to the Crystallographic Theory of Martensite [2], these grains are oriented to produce relatively small axial transformation strain in tension in NiTi compared to e.g., [1 1 1] and [1 1 0] oriented grains.

orientation is identified as the key microstructural factor in influencing the local strain response in the case of S550. Thus in the S550 specimen:

Presence of holes lead to stress concentrations, which then caused strain localization of up to 3% in V-shaped bands.

Microstructure affected the local strain distribution. Specifically, grains that are unfavorably oriented for phase transformation, lead to smaller strains even in the regions where a stress concentration is present due to the holes. Additionally, similar to MONOLITH, the interaction between the grains introduced a gradual onset of phase transformation.

4.1.3. Strain distribution in S150 is determined by the microstructural factors

The strain measurements for S150 specimen show a strong departure from the observation for S550. Despite the availability of sites for stress concentration, S150 does not show distinct strain bands (Fig. 4) and the simulated strain bands in S150 are lower in strain magnitude compared to S550 simulation results.

To compare the structural effect of the holes in S550 and S150, analytical calculations based on the tabulated stress concentration formulae [47] are performed on the samples. The peak stress for a sample with thickness t is calculated as a product of the theoretical stress concentration factor (k_t) and the nominal stress (σ_{nom}), based on the reduced cross sectional area due to the holes, in two separate cases:

(i) a single hole of diameter d in an infinitely long specimen with a fixed width D

$$k_t = 3.000 - 3.140(d/D) + 3.667(d/D)^2 - 1.527(d/D)^3 \quad (1)$$

(ii) a pair of holes of diameter d separated by L in an infinite solid

$$k_t = 3.000 - 0.712(d/L) + 0.271(d/L)^2 \quad (2)$$

The nominal stress, normalized to the uniaxial tensile load P, in both the cases is

$$\sigma_{nom}/P = 1/(t(D-d)) \quad (3)$$

The normalized peak stresses for S150 based on cases **(i)** and **(ii)** are **1.68** and **1.58** respectively. For the S550 specimen, the normalized peak stresses based on cases **(i)** and **(ii)** are **2.37** and **2.51** respectively. This shows that the structural stress concentrations are more prominent in the S550 sample as compared to the S150 sample. The presence of more prominent strain bands in S550 can be rationalized based on the higher stress concentration around the holes in the S550 sample. Just the lower stress concentration in the S150 sample however, cannot be used to completely rationalize the absence of strain bands. This suggests that causes of microstructural origin dominate over the structural stress concentration in determining the local strain distribution.

In S150, the grains have a uniform size distribution and the texture is random, as shown by the EBSD grain maps in Fig. 5(b). Thus, grain structure alone is not the cause behind the absence of strain concentration bands. Further microstructural analysis reveals that precipitates may have played a role in determining the local deformation patterns in S150. Based on the heat treatment employed on the samples (as described in Section 2.1), specifically the 773 K, 1800 s annealing between heavy steel plates, Ni_4Ti_3 precipitates are expected to form in the S150 specimen. Khalil-Allafi et al. [48] observed such precipitation in Ti-50.7at%Ni annealed at 773 K for 3600 s under stresses up to 20 MPa. TEM analysis from a FIB lift-out from a region between the holes as shown in Fig. 7(a, b) shows the presence of precipitates and R-phase. Fig. 7(c, d) show the corresponding bright-field TEM micrograph

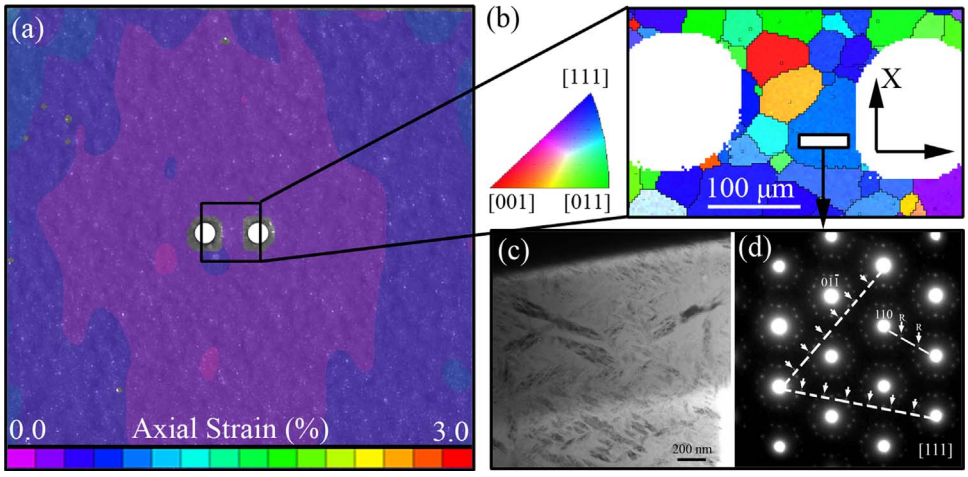

Fig. 7. S150 specimen. (a) Experimental axial strain at peak load, as obtained from DIC. (b) EBSD map of region highlighted in (a), colored according to orientations with respect to the X axis. The FIB cross-sectional cut is indicated by solid black lines. (c) Bright field TEM micrograph of the specimen and (d) the corresponding SAD pattern showing the $\langle 111\rangle_{B2}$ zone axis containing R-phase reflections of type $1/3\langle 110\rangle$, along with $1/7\langle 321\rangle$ reflections of Ni_4Ti_3 precipitate.

and selected area diffraction patterns (SADP). The presence of Ni_4Ti_3 precipitates and R-phase is confirmed based on the $1/7\langle 321\rangle$ and $1/3\langle 110\rangle$ super-reflections, respectively. These observations are consistent with the work of Michutta et al. [49], who observed the precipitation of Ni_4Ti_3 in Ni-rich NiTi during aging under compressive loads up to 50 MPa and the preferential nucleation of R-phase at the precipitate-matrix boundary while cooling. Similarly, Xie et al. [50], empirically observed that the precipitate-matrix boundaries acted as preferred nucleation sites for the martensite phase. The cause for this selective nucleation of the R-phase was investigated by Zhou et. al. [51], who established that Ni_4Ti_3 precipitates act as stress concentrators causing preferential nucleation at the interface of the precipitate with the austenite matrix by numerically estimating the magnitude of stress variation along the interface.

Thus, precipitate-assisted nucleation of martensite and R-phase at various locations in the specimen gage, coupled with a lower stress concentration near the holes compared to S550 and stress concentration around the precipitates, is likely to have resulted in a more uniform strain distribution at peak load in S150. While S550 specimen is also expected to have precipitates, since it underwent an identical heat treatment, the effect of precipitate-assisted nucleation in that case is expected to be secondary to the larger stress concentrations around the holes. In the MONOLITH specimen on the other hand, due to the absence of stress concentration sites (i.e., holes) the effect of precipitates, if any, is indistinguishable from the homogenized response over many thousands of grains. Thus in the S150 specimen:

Presence of holes did not appear to play a role in determining the local strain distribution.

Microstructure determined the local strain distribution. Specifically, the presence of uniformly distributed Ni_4Ti_3 precipitates assisted the nucleation of martensite and the secondary phase, leading to a more uniform strain distribution around the holes on loading at room temperature.

This analysis shows that the microstructure played a progressively more important role in determining the strain response from MONOLITH to S150. Since the same heat treatment is employed in all three samples, the precipitate distribution is expected to be similar. The relative size of the structural features however, decreased from MONOLITH to S150. In the gage section of MONOLITH there are thousands of grains present. In S550, there are approximately 60 grains between the holes. In S150, there are less than 10 grains between the holes. The precipitate size and separation is of the nanometer-scale, as shown in Fig. 7(c), yet it dominated the strain response in S150. Thus, we propose a criterion for selecting phenomenological vs. microstructural models for capturing local strain response around structural features in SMAs based on two factors – the structural feature size relative to the average grain size and the presence of other microstructural features such as precipitates.

4.2. Suitability of micromechanical vs. macro-scale models for SMAs

The discussion in the previous subsection points to the increased influence of microstructural effects as the machined feature size is systematically reduced. For example, in MONOLITH, the local deformation is completely determined by the imposed boundary conditions. In S550, where the feature size is approximately 6 times the average grain size, the deformation is partially influenced by the microstructure. However, when the region of interest contains a few grains as in S150, and when other microstructural features such as precipitates that can affect the nucleation and growth of martensite are present, the local strain response is dominated by the microstructure. Thus we propose that –

- Macro-scale, phenomenological models can adequately capture the local deformation response when the region of interest is larger than 10 times the mean grain size.
- Micromechanical models are necessary to capture the local deformation response in SMAs, when the region of interest is comparable to the mean grain size and when features such as precipitates are present that can modify the spatial distribution of martensite.

This conclusion however has certain exceptions. For example, the regions that are *far enough* from the structural features or stress concentration sites may not experience the effect of local heterogeneities. This is similar to the Saint-Venant's principle, where the local distribution of the loads does not significantly influence the deformation in the regions sufficiently away from where the loads are applied. This points towards the presence of a critical neighborhood around the structural inhomogeneities where microstructural information is essential to reasonably predict the local deformation response. However, in regions away from the holes for example, phenomenological models that do not account for the microstructural heterogeneities continue to be adequate, as long as the regions interrogated contain a large number of grains. Also, when the region of interest is large, the local influence of precipitates or inclusions is small.

This discussion is relevant to predicting the response in small SMA assemblies like micron sized actuators and sensors, and porous structures, where the relative sizes of structural features (like pores) are comparable to the length scale of the intrinsic microstructure of the material. In such cases the above criterion can be useful in selecting an appropriate macro scale model or a microstructural model.

5. Conclusions

In this work we examined a structural feature size effect on the local deformation in a NiTi SMA by studying three contrasting cases with varying sizes of machined holes with respect to the average grain size in planar specimens. This study details the deformation behavior using extensive characterization on three specific specimen cases which reflect the extremes of hole (feature) size with respect to the grain (microstructure) size. Even though NiTi is used as a model system, these results are expected to apply to other SMAs as well.

1. In the absence of structural features or stress concentration sites, the deformation is homogeneous to a global strain of 0.75%, as seen in the MONOLITH specimen. The axial strain distribution, simulated using a macro-scale, phenomenological model for phase transformation is adequate to capture the uniform strains seen in the experiment.
2. In a specimen where the grain size is relatively small compared to the hole size, structural effects dominate over microstructural effects, as seen in the S550 specimen. Individual grains influence the local strain distributions, e.g., grains unfavorably oriented for transformation interrupting a strain band in the region of stress concentration.
3. In the specimens such as S150 where stress concentration around the holes is diminished, the holes are comparable in size to the grains, and feature such as precipitates are present that can modify the martensite nucleation and growth mechanics, the microstructural effects dominate over structural effects. In these cases, the local strain distribution significantly deviates from the prediction of the macro-scale model, where the predicted stress concentration around the holes does not reflect in the actual axial strain observations.
4. Microstructural models are more appropriate to predict local phase transformation response when the region of interest or a structural feature in the specimen is less than ten times in size compared to the average grain size, or when precipitates can influence local martensite nucleation and growth. When a multitude of grains are

present in the region of interest, a macro-scale model is adequate for predicting the local phase transformation response.

In the future, this work will be well complimented by an approach that characterizes a larger number of samples to provide statistical insights into the interaction between machined features and local phase transformation response. An efficient way to do this is using micromechanical modeling, which takes experimental microstructural characterization as an input to predict grain and sub-grain scale deformation in virtual samples.

Acknowledgements

The authors would like to acknowledge the use of NUANCE (NSF ECCS-1542205) and MatCI (NSF DMR-1121262) facilities at Northwestern University and financial support from Department of Energy, Office of Basic Energy Science (Grant no. DE-SC0010594).

References

[1] M.S. Wechsler, D.S. Lieberman, T.A. Read, On the theory of the formation of martensite, Trans. AIME 197 (1953) 1503–1515.
[2] K. Bhattacharya, Microstructure of Martensite: Why it Forms and How it Gives Rise to the Shape-memory Effect, Oxford University Press, 2003.
[3] D.A. Miller, D.C. Lagoudas, Influence of cold work and heat treatment on the shape memory effect and plastic strain development of NiTi, Mater. Sci. Eng. a-Struct. Mater. Prop. Microstruct. Process. 308 (2001) 161–175.
[4] K. Gall, J. Tyber, G. Wilkesanders, S.W. Robertson, R.O. Ritchie, H.J. Maier, Effect of microstructure on the fatigue of hot-rolled and cold-drawn NiTi shape memory alloys, Mater. Sci. Eng.: A 486 (2008) 389–403.
[5] K. Otsuka, X. Ren, Physical metallurgy of Ti- Ni-based shape memory alloys, Progr. Mater. Sci. 50 (2005) 511–678.
[6] M.A.M. Bourke, R. Vaidyanathan, D.C. Dunand, Neutron diffraction measurement of stress-induced transformation in superelastic NiTi, Appl. Phys. Lett. 69 (1996) 2477–2479.
[7] M.A.M. Bourke, D.C. Dunand, Phase fraction, texture and strain evolution in superelastic NiTi and NiTi-TiC composites investigated by neutron diffraction, Acta Mater. 47 (1999) 3353–3366.
[8] S. Cai, J.E. Schaffer, C. Yu, M.R. Daymond, Y. Ren, Evolution of intergranular stresses in a martensitic and an austenitic niti wire during loading-unloading tensile deformation, Metall. Mater. Trans. A 46 (2015) 2476–2490.
[9] S. Rajagopalan, A.L. Little, M.a.M. Bourke, R. Vaidyanathan, Elastic modulus of shape-memory NiTi from in situ neutron diffraction during macroscopic loading, instrumented indentation, and extensometry, Appl. Phys. Lett. 86 (2005) 081901.
[10] S. Qiu, B. Clausen, S.A. Padula, R.D. Noebe, R. Vaidyanathan, On elastic moduli and elastic anisotropy in polycrystalline martensitic NiTi, Acta Mater. 59 (2011) 5055–5066.
[11] A.P. Stebner, D.W. Brown, L.C. Brinson, Young's modulus evolution and texture-based elastic-inelastic strain partitioning during large uniaxial deformations of monoclinic nickel-titanium, Acta Mater. 61 (2013) 1944–1956.
[12] A.P. Stebner, S.C. Vogel, R.D. Noebe, T.A. Sisneros, B. Clausen, D.W. Brown, A. Garg, L.C. Brinson, Micromechanical quantification of elastic, twinning, and slip strain partitioning exhibited by polycrystalline, monoclinic nickel-titanium during large uniaxial deformations measured via in-situ neutron diffraction, J. Mech. Phys. Solids 61 (2013) 2302–2330.
[13] S.M. Ueland, C.A. Schuh, Transition from many domain to single domain martensite morphology in small-scale shape memory alloys, Acta Mater. 61 (2013) 5618–5625.
[14] D.M. Norfleet, P.M. Sarosi, S. Manchiraju, M.F.X. Wagner, M.D. Uchic, P.M. Anderson, M.J. Mills, Transformation-induced plasticity during pseudoelastic deformation in Ni-Ti microcrystals, Acta Mater. 57 (2009) 3549–3561 (12 bibtex: Norfleet2009).
[15] J. Ye, R.K. Mishra, A.R. Pelton, A.M. Minor, Direct observation of the NiTi martensitic phase transformation in nanoscale volumes, Acta Mater. 58 (2010) 490–498.
[16] J. San Juan, M.L. Nó, C.A. Schuh, Thermomechanical behavior at the nanoscale and size effects in shape memory alloys, J. Mater. Res. 26 (2011) 2461–2469.
[17] J.E. Schaffer, Structure-property relationships in conventional and nanocrystalline niti intermetallic alloy wire, J. Mater. Eng. Perform. 18 (2009) 582–587.
[18] C. Frick, S. Orso, E. Arzt, Loss of pseudoelasticity in nickel-titanium sub-micron compression pillars, Acta Mater. 55 (2007) 3845–3855.
[19] T. Waitz, T. Antretter, F.D. Fischer, H.P. Karnthaler, Size effects on martensitic phase transformations in nanocrystalline NiTi shape memory alloys, Mater. Sci. Technol. 24 (2008) 934–940.
[20] L.C. Brinson, One-dimensional constitutive behavior of shape memory alloys: thermomechanical derivation with non-constant material functions and redefined martensite internal variable, J. Intell. Mater. Syst. Struct. 4 (1993) 229–242.
[21] J.G. Boyd, D.C. Lagoudas, Constitutive model for simultaneous transformation and reorientation in shape memory materials, Appl. Mech. Div. 189 (1994) 159–172.
[22] A. Bekker, L.C. Brinson, Temperature-induced phase transformation in a shape memory alloy: phase diagram based kinetics approach, J. Mech. Phys. Solids 45 (1997) 949–988.
[23] M. Panico, L.C. Brinson, A three-dimensional phenomenological model for martensite reorientation in shape memory alloys, J. Mech. Phys. Solids 55 (2007) 2491–2511.
[24] D.J. Hartl, D.C. Lagoudas, Simultaneous Transformation and Plastic Deformation in Shape Memory Alloys, (2008).
[25] C. Morin, Z. Moumni, W. Zaki, Thermomechanical coupling in shape memory alloys under cyclic loadings: experimental analysis and constitutive modeling, Int. J. Plast. 27 (2011) 1959–1980 (Bibtex:Morin2011).
[26] Y. Chemisky, A. Duval, E. Patoor, T. Ben Zineb, Constitutive model for shape memory alloys including phase transformation, martensitic reorientation and twins accommodation, Mech. Mater. 43 (2011) 361–376 (WOS:000292677500002 bibtex: Chemisky2011).
[27] A. Kelly, A.P. Stebner, K. Bhattacharya, A micromechanics-inspired constitutive model for shape-memory alloys that accounts for initiation and saturation of phase transformation, J. Mech. Phys. Solids (2016).
[28] E. Patoor, A. Eberhardt, M. Berveiller, Micromechanical modelling of the shape behavior, Appl. Mech. Div. 189 (1994) 23–37.
[29] D. Entemeyer, E. Patoor, A. Eberhardt, M. Berveiller, Micromechanical modelling of the superthermoelastic behavior of materials undergoing thermoelastic phase transition, J. Phys. IV 5 (1995) 233–238.
[30] P. Thamburaja, L. Anand, Polycrystalline shape-memory materials: effect of crystallographic texture, J. Mech. Phys. Solids 49 (2001) 709–737.
[31] S. Manchiraju, P.M. Anderson, Coupling between martensitic phase transformations and plasticity: a microstructure-based finite element model, Int. J. Plast. 26 (2010) 1508–1526.
[32] A.W. Richards, R.A. Lebensohn, K. Bhattacharya, Interplay of martensitic phase transformation and plastic slip in polycrystals, Acta Mater. 61 (2013) 4384–4397 (WOS:000321086100009 bibtex: Richards2013).
[33] H.M. Paranjape, S. Manchiraju, P.M. Anderson, A phase field - Finite element approach to model the interaction between phase transformations and plasticity in shape memory alloys, Int. J. Plast. 80 (2016) 1–18.
[34] P. Zhu, A.P. Stebner, L.C. Brinson, A numerical study of the coupling of elastic and transformation fields in pore arrays in shape memory alloy plates to advance porous structure design and optimization, Smart Mater. Struct. 22 (2013) (WOS:000323832000011 bibtex: Zhu2013).
[35] C. Bewerse, K.R. Gall, G.J. McFarland, P. Zhu, L.C. Brinson, Local and global strains and strain ratios in shape memory alloys using digital image correlation, Mater. Sci. Eng.: A 568 (2013) 134–142.
[36] H. Paranjape, P.M. Anderson, Texture and grain neighborhood effects on Ni-Ti shape memory alloy performance, Model. Simul. Mater. Sci. Eng. 22 (2014) 075002.
[37] M. Kimiecik, J. Wayne Jones, S. Daly, Grain orientation dependence of phase transformation in the shape memory alloy Nickel- Titanium, Acta Mater. 94 (2015) 214–223.
[38] H.M. Paranjape, P.P. Paul, H. Sharma, P. Kenesei, J.-S. Park, T. Duerig, L.C. Brinson, A.P. Stebner, Influences of granular constraints and surface effects on the heterogeneity of elastic, superelastic, and plastic responses of polycrystalline shape memory alloys, J. Mech. Phys. Solids 102 (2017) 46–66.
[39] S. Daly, A. Miller, G. Ravichandran, K. Bhattacharya, An experimental investigation of crack initiation in thin sheets of nitinol, Acta Mater. 55 (2007) 6322–6330.
[40] K. Kim, S. Daly, Martensite strain memory in the shape memory alloy nickel-titanium under mechanical cycling, Exp. Mech. 51 (2011) 641–652.
[41] ASTME8 / E8m-15a, Standard Test Methods for Tension Testing of Metallic Materials, 2015. URL ⟨http://www.astm.org⟩.
[42] S. Daly, G. Ravichandran, K. Bhattacharya, Stress-induced martensitic phase transformation in thin sheets of Nitinol, Acta Mater. 55 (2007) 3593–3600.
[43] T. Merzouki, C. Collard, N. Bourgeois, T. Ben Zineb, F. Meraghni, Coupling between measured kinematic fields and multicrystal SMA finite element calculations, Mech. Mater. 42 (2010) 72–95.
[44] A.P. Stebner, L.C. Brinson, Explicit finite element implementation of an improved three dimensional constitutive model for shape memory alloys, Comput. Methods Appl. Mech. Eng. 257 (2013) 17–35.
[45] H. Yin, Y. He, Z. Moumni, Q. Sun, Effects of grain size on tensile fatigue life of nanostructured niti shape memory alloy, Int. J. Fatigue 88 (2016) 166–177.
[46] L.C. Brinson, I. Schmidt, R. Lammering, Stress-induced transformation behavior of a polycrystalline NiTi shape memory alloy: micro and macromechanical investigations via in situ optical microscopy, J. Mech. Phys. Solids 52 (2004) 1549–1571 (7 bibtex: Brinson2004).
[47] W.D. Pilkey, D.F. Pilkey, Holes, John Wiley & Sons, Inc., 2008, pp. 176–400.
[48] J. Khalil-Allafi, A. Dlouhy, G. Eggeler, Ni4ti3-precipitation during aging of NiTi shape memory alloys and its influence on martensitic phase transformations, Acta Mater. 50 (2002) 4255–4274.
[49] J. Michutta, C. Somsen, A. Yawny, A. Dlouhy, G. Eggeler, Elementary martensitic transformation processes in ni-rich niti single crystals with ni4ti3 precipitates, Acta Materialia 54 (2006) 3525 - 3542. Selected Papers from the Meeting Micromechanics and Microstructure Evolution: Modeling, Simulation and Experiments held in Madrid/Spain, 11-16 September 2005.
[50] C.Y. Xie, L.C. Zhao, T.C. Lei, Effect of Ti3ni4 precipitates on the phase transitions in an aged Ti-51.8at% Ni shape memory alloy, Scr. Metall. Mater. 24 (1990) 1753–1758.
[51] N. Zhou, C. Shen, M.F.X. Wagner, G. Eggeler, M.J. Mills, Y. Wang, Effect of Ni(4)Ti (3) precipitation on martensitic transformation in Ti-Ni, Acta Mater. 58 (2010) 6685–6694 (20 bibtex: Zhou2010).